Magnetocardiography measurements with ^{4}He vector optically pumped magnetometers at room temperature

S. Morales, M.C. Corsi, W. Fourcault, F. Bertrand, G. Cauffet, C. Gobbo, F. Alcouffe, F. Lenouvel, M. Le Prado, F. Berger, et al.

Magnetocardiography measurements with ^{4}He vector optically pumped magnetometers at room temperature

Magnetocardiography measurements with ^{4}He vector optically pumped magnetometers at room temperature

S. Morales [1*], M.C. Corsi[1*], W. Fourcault [1], F. Bertrand[1], G. Cauffet[2], C. Gobbo[1], F. Alcouffe[1], F. Lenouvel[1], M. Le Prado[1], F. Berger[1], G. Vanzetto[3,4] and E. Labyt[1]

1. CEA, LETI, MINATEC Campus, F-38054 Grenoble, France
2. Univ. Grenoble Alpes, G2Elab, F-38000 Grenoble, France; CNRS, G2Elab, F-38000 Grenoble, France
3. Department of Cardiology, University Hospital, Grenoble, France
4. INSERM U1039, Bioclinic Radiopharmaceutics Laboratory, Grenoble, France

* These authors contributed equally to this work

E-mail: corresponding author sophie.morales@cea.fr

In this paper, we present a proof of concept study which demonstrates for the first time the possibility to record magnetocardiography (MCG) signals with ^{4}He vector optically-pumped magnetometers (OPM) operated in a gradiometer mode. Resulting from a compromise between sensitivity, size and operability in a clinical environment, the developed magnetometers are based on the parametric resonance of helium in zero magnetic field. Sensors are operated at room-temperature and provide a tri-axis vector measurement of the magnetic field. Measured sensitivity is around 210 fT/√Hz in the bandwidth [2 Hz; 300 Hz]. MCG signals from a phantom and two healthy subjects are successfully recorded. Human MCG data obtained with the OPMs are compared to reference electrocardiogram (ECG) recordings: similar heart rates, shapes of the main patterns of the cardiac cycle (P/T waves, QRS complex) and QRS widths are obtained with both techniques.

Keywords: Optically Pumped Magnetometers (OPM), helium, Magnetocardiography (MCG)

1. Introduction

Magnetocardiography is a contactless, non-invasive imaging technique which consists in measuring the magnetic fields generated by the heart, about one million times smaller than the Earth's magnetic field. Electrocardiography (ECG) and magnetocardiography (MCG) both demonstrate a high temporal resolution. However, discontinuities of the electrical conductivity in body tissues (bones, fat layer) act as a low pass spatial filter of electrical cardiac signals recorded in ECG. As a result, a current flowing from a localized cardiac region produces an ECG effect at almost all surface electrodes. Consequently, it is difficult to interpret spatial information like QT dispersion in ECG while multi-channels MCG should allow a more sensitive assessment of the cellular dispersion of ventricular repolarization (Antzelevitch et al., 1998). Multi-channels MCG are also useful to detect precordial magnetic fields originating from many sites over the heart with a high signal to noise ratio and a good spatio-temporal resolution (Ikefuji et al., 2007). Another advantage of MCG is its ability to detect the magnetic field produced by intracellular and extracellular currents in cardiac tissue, while ECG only detects the effects of currents flowing through the body tissue (Wikswo and Barach, 1982)(Koch and Haberkorn, 2001). Recent clinical trials have reported that MCG mapping is useful for identifying spatial current dispersion patterns, as well as for characterizing and discriminating Brugada syndrome and complete right bundle branch block (Kandori et al., 2004). MCG mapping has also been reported to provide a higher statistical sensitivity than ECG, giving the opportunity to better diagnose cardiac arrhythmia and coronary artery diseases (Fenici et al., 2013)(Kwong et al., 2013)(Park et al., 2005). MCG can also play a critical role in the diagnosis of long QT syndrome in fetuses (Cuneo et al., 2013). MCG systems are currently based on the use of ultra-sensitive Superconducting Quantum Interference Devices (SQUIDs), with only one magnetic sensitive direction characterized by a magnetic sensitivity

of about 1-10 fT/√Hz (Sternickel and Braginski, 2006). Nevertheless, dissemination of this imaging technique is hindered by the high cost of SQUID equipment both in terms of initial investment (more than one M€), as well as operational constraints and maintenance cost (more than 100 k€/year). Moreover due to the cryogenic cooling system based on helium, a thermal insulation layer of a few centimeters is required between the skin and the detector: magnetic signal strength is thus reduced. As a result, despite its clinical interest, SQUID based magnetocardiography is not widespread in hospitals.

Several emerging sensors dedicated to the measurements of low magnetic fields have been developed during the past few years (Pannetier-Lecoeur et al., 2011) (Livanov et al., 1981). Among them, cryogenic-free Optically-Pumped Magnetometers (OPM) have emerged as a promising alternative to SQUIDs detector (Knappe et al., 2010). High sensitivity OPMs tested in the past are all based on a vapor of alkali atoms and exploit the optical and magnetic properties of paramagnetic alkali atoms. The most commonly used architectures of alkali OPM in the MCG field are Mx magnetometers (Bison, 2004) and the so-called Spin-Exchange Relaxation-Free (SERF) magnetometers (Wyllie et al., 2012), (Shah and Wakai, 2013). Both of them have only one sensitive axis. MCG mapping has been carried out with an array of 83 Mx magnetometers in a second-order gradiometer configuration: achieved sensitivity is around 1 pT/√Hz in the frequency range 1-10 Hz (Bison et al., 2009) (Bison et al., 2010) (Lembke et al., 2014). Better sensitivities are demonstrated in the SERF regime at the expense of the dynamic range of the sensor (since SERF regime is attained only close to zero magnetic field) and higher operating temperature – typically around 150°C which imposes a thermal insulation layer between the sensor and the skin (Xia et al., 2006). In real clinical environment, demonstrated sensitivity of SERF prototypes is comprised between 10-100 fT/√Hz in the frequency range of interest for MCG (0.5-50 Hz). Fetal MCG measurements have recently been performed with an array of these alkali OPMs (Alem et al., 2015) (Wyllie, 2012).

In this paper, the possibility to record MCG signals with room-temperature vector OPMs based on helium atoms is demonstrated for the first time. A significant advantage of helium 4 is that it does not require cooling nor heating to be in a gas phase as needed for sensor operation. This avoids the use of thermal insulation and, consequently allows reducing the distance between the sensor and the subject. So, the signal strength is increased. The vector measurement should also allow recording magnetic fields coming from all cardiac source orientations. This should solve one of the current limitation of multichannel MCG systems (with only one magnetic sensitive direction) which are more sensitive to tangential cardiac sources while multichannel ECG mapping is more sensitive to radial and posterior cardiac sources (Mäntynen et al., 2014). In order to demonstrate the potential of ^{4}He optically-pumped magnetometers, we recorded simulated MCG signals generated by a phantom and real MCG signals from two healthy subjects. Human MCG data have been cross-validated with ECG recordings with comparison of the main features of the cardiac cycle namely heart rate, QRS width and QT interval. This proof-of-concept study - with two ^{4}He magnetometers operated in a gradiometer mode – paves the way towards the development of a MCG system based on an array of ^{4}He optically pumped magnetometers dedicated to MCG imaging.

2. Materials and methods : ^{4}He optically pumped magnetometer

2.1. Physical principle

The physical principle of operation of our OPM – based on optical pumping and parametric resonance of ^{4}He metastable atoms in a near-zero magnetic field – is sketched in Figure 1 (Le Prado, 2014). A HF discharge brings ^{4}He atoms from the fundamental state, insensitive to the Zeeman effect, to the 2^3S_1 metastable state, where radiative decay back to the fundamental level is forbidden, which makes this state relatively long-lived. The magnetic field B_0 splits the 2^3S_1 level into three Zeeman sublevels. At the thermodynamic equilibrium, metastable atoms are almost equally distributed within the three sublevels and no resonance signal can be detected. In order to amplify and measure the resonance signal, an alignment of magnetic moments is created by optical pumping with a linearly

polarized light tuned on the D_0 line (wavelength of 1083 nm): in this configuration, the alignment is collinear to the $\vec{E}_0$ field of the light polarization.

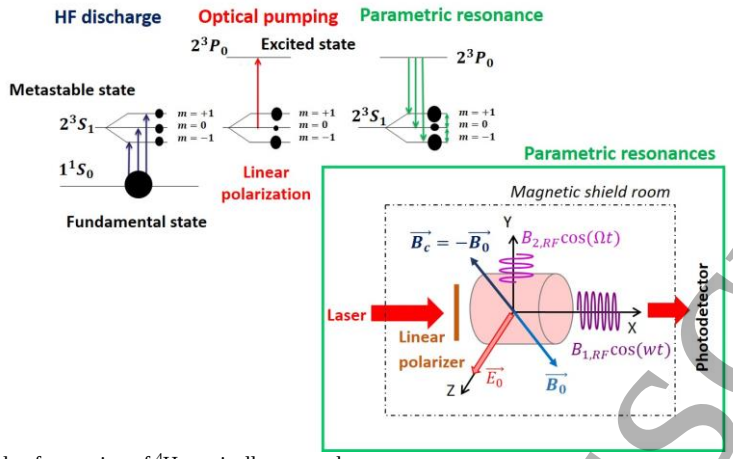

Figure 1: Simplified principle of operation of ^{4}He optically pumped magnetometer.

At low magnetic fields ($B_0 \ll \Gamma/\gamma$ with Γ the relaxation rate of metastable atoms and γ the gyromagnetic ratio of 4He atoms), and when the alignment direction is transverse to the field, a narrow resonance is observed when sweeping $\vec{B}_0$ around the zero field value (a phenomenon known as the Hanle effect (Cohen-Tannoudji et al., 1970b)). The maximum transmitted light through the vapor cell is measured when the magnetic field is strictly equal to zero. Similar resonances can be detected when a radio-frequency (RF) magnetic field - transverse to the pumping direction set by the direction of the polarization $\vec{E}_0$ - is added. These resonances, called parametric resonances, are sensitive to first order only to the component of $\vec{B}_0$ collinear to the RF (Cohen-Tannoudji et al., 1970a)(Dupont-Roc et al., 1969). To measure the three components of the magnetic field, Dupont-Roc pioneered a configuration based on two orthogonal RF magnetic fields $\vec{B}_{1,RF}$ and $\vec{B}_{2,RF}$, both transverse to the pumping direction (Dupont-Roc, 1971).

The ^{4}He magnetometer described in this publication is based on this configuration. The two RF fields $\vec{B}_{1,RF}$ and $\vec{B}_{2,RF}$ - with frequencies $w/2\pi = 9$ kHz and $\Omega/2\pi = 40$ kHz - are respectively applied along the X and Y axis and are orthogonal to the linear polarization of the pump beam $\vec{E}_0$ applied along z-axis. The frequencies of the RF fields are chosen so as to satisfy the following condition $w_L \ll \Gamma < \Omega \ll w$ with w_L the Larmor pulsation of the near-zero external magnetic field $\vec{B}_0$ (the modulation must be fast enough so that the spins cannot adiabatically follow the modulation). Frequencies are also chosen so as to reduce the intensity noise of the pump laser beam which is minimum between 4 kHz – 45 kHz. To provide a wide dynamic range, a compensation field $\vec{B}_c$ opposed to the ambient magnetic field $\vec{B}_0$ - is applied through a closed-control-loop system that locks the magnetometer to the precisely equal zero magnetic field. The error signal is provided by demodulation of the transmitted laser light at the pulsations w, Ω and $\Omega \pm w$ as explained in (Dupont-Roc, 1970). The value and direction of the $\vec{B}_0$ field are deduced from the current injected in the compensation coils.

2.2. Description of the experimental layout

Figure 2.a describes the experimental setup: magnetometers are operated inside a magnetic shielded room and a gradiometer configuration with two ^{4}He OPMs is used. One sensor (hereinafter referred to as OPM_1) is placed just above the chest of the subject. It measures the MCG signal of interest and the residual field inside the magnetic shielded room. The second sensor (hereinafter referred to as OPM_2),

located 30 cm away from the first, measures only the residual field. All the MCG measurements presented here have been obtained along the Y-axis, since the magnetic field of the heart is mainly orthogonal to the chest. Synchronous demodulations at w, Ω and $\Omega \pm w$ are performed at the level of each sensor by a dedicated analog electronic card. Demodulated signals are recorded and subtracted by the OROS 3-Series/NVGate® acquisition software (OROS, 2009). This gradiometer configuration allows monitoring and removing the ambient residual magnetic field inside the magnetic shielded room.

A single ^{4}He magnetometer is shown in Figure 2.b. The cylindrical glassblown cells - with 1cm height and diameter - are filled to 20 Torrs of high purity helium. The optimal pressure is determined using a numerical model (Rutkowski et al., 2014). Compensation field and RF fields are applied using tri-axis square Helmholtz coils (outside dimensions 1.7 cm). The amplitudes of the applied RF fields are adjusted so as to optimize the sensitivity of the magnetometer and set to 1.5 µTpp for the 40 kHz RF field and 120 nTpp for the 9 kHz RF field.

The whole system is designed to minimize the distance between the source (i.e. the heart) and the sensitive element of the magnetometer (i.e. the gas cell). The cubic support for the field coils is inserted in an opening of a printed circuit board, so as to minimize as much as possible the distance between the sensitive element of the sensor and the heart. Thanks to this optimized configuration, the average distance between the center of the gas cell and the skin is less than 1 cm, and the distance between the bottom part of the cubic support and the skin is less than 5 mm. This is substantially shorter that the distance between a SQUID coil and the skin. This compact configuration – permitted by the lack of heating or cooling system – is one of the advantages of 4He OPM over other available technologies (i.e. SQUID or alkali based OPM).

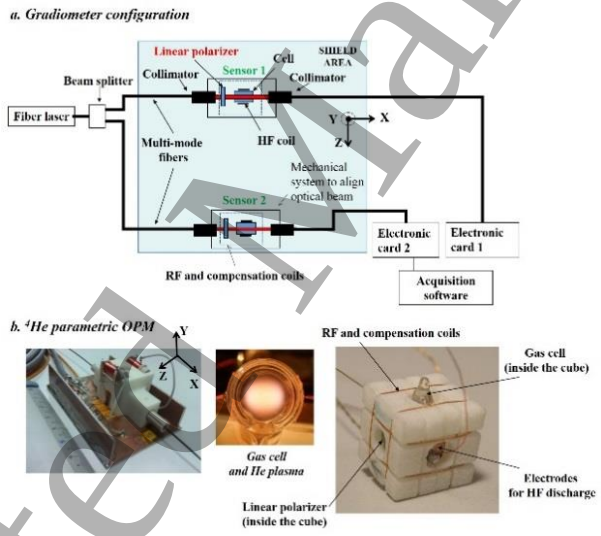

Figure 2: a. Schematic drawing of the tested configuration. The bold (thin) line represents optical (electrical) connections. b. Overview of a single magnetometer containing a 1 cm sided glass blown cell, filled with 20 Torrs of high purity ^{4}He (helium discharge inside the gas cell is maintained at about 40 mW of forward HF power) and structure of the RF/compensation coils (tri-axis square Helmholtz coils).

The pump laser is a key sub-system of the sensor. It relies on a fiber laser architecture including a pump laser diode, a Wavelength Division Multiplexer (WDM), an Yb doped Fiber Bragg Grating (FBG), an optical isolator and a splitter to allow a feedback control (Fourcault et al., 2010). A noise reduction feedback loop is implemented resulting in a relative intensity noise (RIN) in the order of $-130\ /-140\ dB/\sqrt{Hz}$ between 4 kHz – 45 kHz. The power of the pump beam is optimized to 1.25 mW and the diameter of the collimated pump beam inside the gas cell is set to 5.4 mm.

The analog electronic card and the laser are set outside the magnetic shielded room and connected to the sensitive element through electrical harnesses and multimode optical fibers. The depolarized pump beam at the output of the collimator is linearly polarized by a linear polarizer located at the input of the gas cell resulting in an atomic alignment of the vapor.

2.3. Demonstrated sensitivity

Sensitivity of the ^{4}He magnetometer has been characterized in a laboratory environment inside the cylindrical five-layer µ-metal passive magnetic shield (length 1.5 m and inner diameter 0.6 m). It was also measured in a clinical environment inside a light two-layer passive magnetic shielded room (MSR) combined with an internal active shielding (Maxshield from Elekta Neuromag®). In both cases, the typical residual magnetic fields inside the shields are 20-30 nT. In the laboratory environment, the measured sensitivity of a single magnetometer is around 210 fT/√Hz between 2 and 300 Hz (bandwidth of the ^{4}He magnetometer is set by electronic regulation to 300 Hz but higher cut-off frequencies could be chosen) (Figure 3). The low-frequency noise increase below 2 Hz is being currently investigated. Sensitivity in clinical environment is somewhat deteriorated at low frequency due to magnetic disturbances induced by the building ventilation.

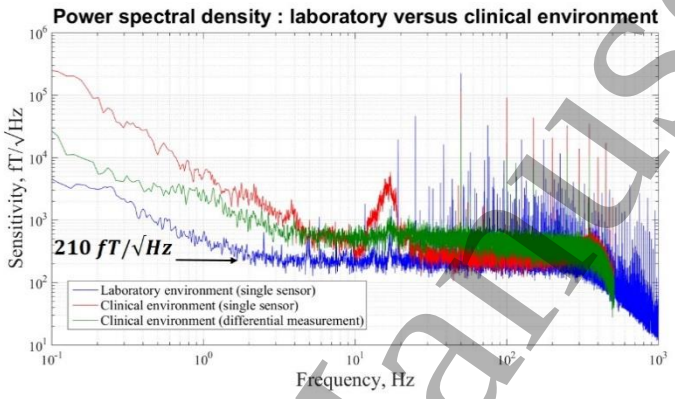

Figure 3: Measured sensitivity of one magnetometer in the laboratory magnetic shield (blue) or inside the magnetically disturbed clinical shielded room (red for one ^{4}He sensor and green for the gradiometer configuration). Our sensors show a 300 Hz bandwidth.

3. Results and discussion

3.1. Phantom measurements

The operability of the ^{4}He OPM was first demonstrated in the laboratory-environment by a simulation study on a MCG phantom. A synthetic ECG signal with realistic PQRST morphology and heart rate dynamics was obtained with the open source ECG waveform generator ECGSYN, from the Physionet Toolbox (McSharry et al., 2003) (PhysioNet, 2015). This periodic ECG set-point is generated by an arbitrary waveform generator that drives a simple coil (circular current loop with 5 turns). The electrical current in the phantom coil produces a reference MCG signal that is recorded by the OPM.

Our phantom coil is characterized by a transfer function of 49.6 pT/V at the level of the OPM_1 located on the axis of the loop at 7.5 cm from the center of the loop. The reference sensor OPM_2 is located in the same horizontal plane XZ at a distance of 10 cm from the OPM1. In what follows, the signal resulting from the multiplication of the voltage ECG set-point by this transfer function will be called "phantom reference signal".

Signal processing applied on MCG data is cross-validated by comparing firstly the averaged unfiltered phantom reference signal with the same filtered signal (data not shown), and secondly by comparing this averaged unfiltered phantom reference signal with the recorded OPM data resulting from the differential measurement between two ^{4}He magnetometers (Figure 4). In both cases, pre-filtering is performed with the same finite impulse response (FIR) bandpass filter [0.15 Hz - 25 Hz]. As shown in Figure 4, the morphology of the MCG cycle (QRS complex, P and T waves) is not distorted by signal processing.

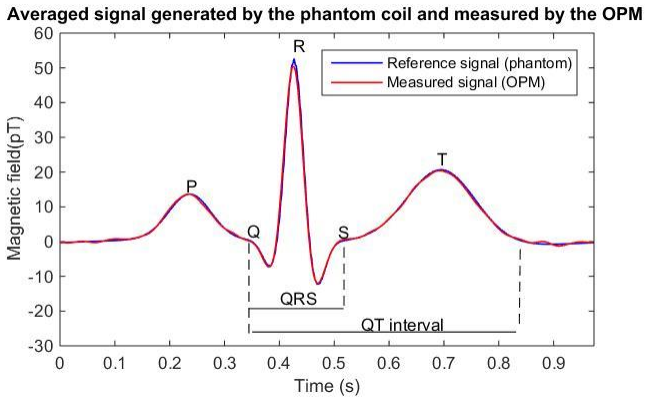

Figure 4: Averaged MCG signal (30 beats) for the unfiltered phantom reference signal and for the differential OPM measurement.

Un-averaged reference and measured signals are subsequently compared (Figure 5 a-b): QRS complex, P and T waves are clearly detected on the real-time measurements recorded by the ^{4}He OPM gradiometer (cf. un-averaged pre-filtered OPM signal - Figure 5-b).

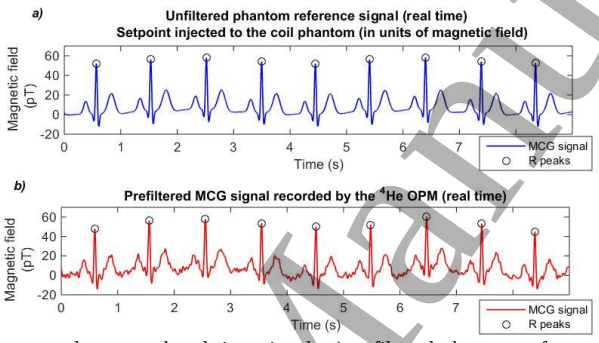

Figure 5: Comparison of the reference and measured real-time signals a) unfiltered phantom reference signal, b) pre-filtered MCG signal deduced from the OPM differential measurement.

Quantitative comparison of the reference and OPM signals is performed through the detection of RR interval (heart rate) and QRS duration following Pan and Tompkins algorithm (Pan and Tompkins, 1985) (Elgendi, 2013): QRS enhancement is performed by pre-filtering the signal with a third order Butterworth bandpass filter in the frequency range [5-15] Hz, followed by differentiation and squaring. QRS detection is then performed by a moving window integration. The width of the integrator window is initialized to the approximate duration of the QRS complex (W=170 ms).

Table 1. Quantitative cardiac parameters for the phantom.

Signal	Heart rate	QRS duration
Reference signal	61.7 beats/min (± 1.0 beats/min)	153 ms (± 0.3 ms)
OPM signal	61.7 beats/min (± 0.9 beats/min)	154 ms (± 1 ms)

Figure 4, Figure 5, Table 1 show that the reference signal from the phantom and the MCG signal recorded by the OPM display the same typical features.

3.2.MCG measurements on healthy volunteers

Successful phantom simulations have been then cross-validated with real MCG-measurements carried out in two healthy subjects (males, 37 and 47 years old) in a magnetic shielded room at Clinatec (Grenoble, France). These recordings have been performed in the frame of the clinical research protocols MAP_EFNI n°2013-A00414-411 and Minimag n°2014-A01136-41 authorized by the

ANSM (Agence Nationale de Sécurité du Médicament et des produits de santé, i.e. French FDA), and ethical committee. ECG and MCG have been simultaneously carried out. Three bipolar ECG leads (V1, V2 and V3 as clinically referenced) were used to perform the reference recordings. During MCG recordings, according to the MCG grid system (Fujino et al., 1984), Sensor 1 (OPM_1) is placed just above the chest of the healthy volunteer, at the level of the fourth intercostal space and on the left of the nipple, corresponding to D4 position on the MCG grid system (Figure 6,b). It measures the MCG signal of interest and the residual field B_R along the Y axis. Distance between the bottom part of S_1 and the chest is set to the smaller value that avoids any contact between skin and the sensor during a normal respiration. It is estimated to be 5 mm in average. Sensor 2 (OPM_2), located at about 30 cm away from S_1, and not above the subject's chest, only measures B_R. Figure 6 presents the set-up of the clinical measurement and the MCG grid system according to (Fujino et al., 1984). Recordings are performed at rest.

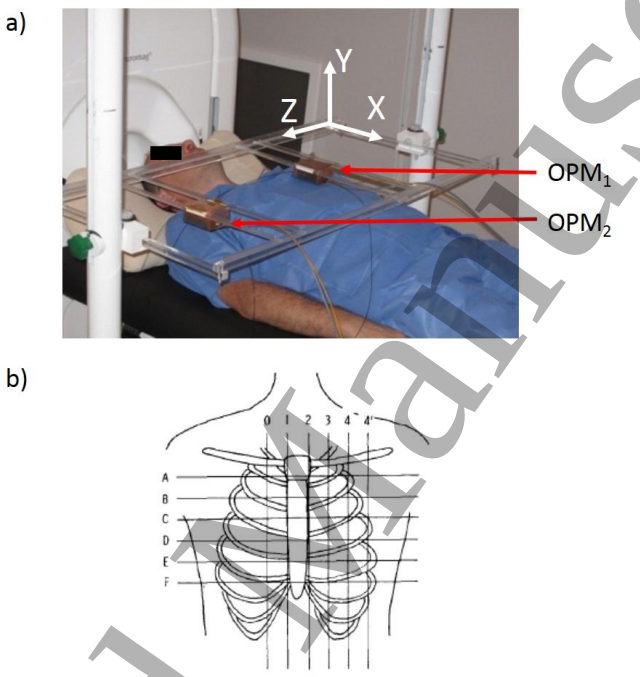

Figure 6: a) General layout with a healthy subject placed in the supine position. OPMs are mounted on a non-magnetic holder and can be translated along the three axes. b) MCG grid system from (Fujino et al., 1984)

Measurements are filtered with a FIR bandpass filter [0.6 Hz - 45 Hz]: cut-off frequencies are adapted to take into account the richer frequency distribution of the physiological human cardiac signal compared to the phantom signal. Time segments of the recorded ECG and OPM data are shown in Figure 7. QRS complexes as well as T-waves are clearly visible in both data sets. P-waves are only visible in the ECG signal. This observation was expected. Indeed, the atrial excitation originates from currents that spread tangentially along the atrial wall (Durrer et al., 1970). As a result, the P wave in MCG is recorded over the left sternal edge at the level of the third or the fourth intercostal space – corresponding to C2 and D2 positions in the Figure 6, b (Takeuchi et al., 1988). Our OPM was placed over the fourth intercostal space but more laterally as described above (D4 position) and so, it mainly records ventricular depolarization/repolarization events.

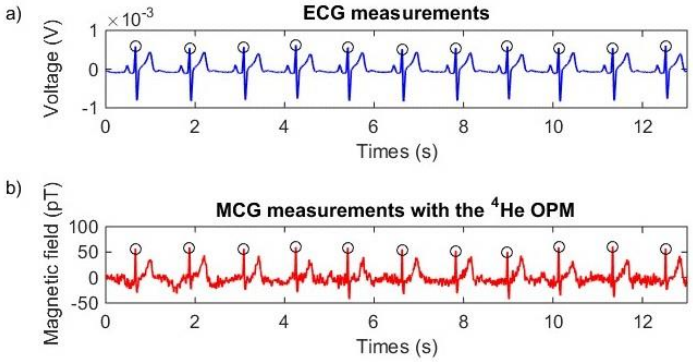

Figure 7: Real-time cardiac signal of the 37 years old healthy subject detected simultaneously with a) ECG electrodes and b) ^{4}He OPM operated in a gradiometer mode.

Heart-rate - determined from the RR intervals on ECG and MCG data– are compared using the simultaneously ECG and OPM recordings on 180 s: both measurements are perfectly superimposed as shown in Figure 8. This is confirmed by a Student t-test (α=0.05): a p-value of 98% was determined which confirms that there is no statistical difference between the heart rate determined with ECG and MCG.

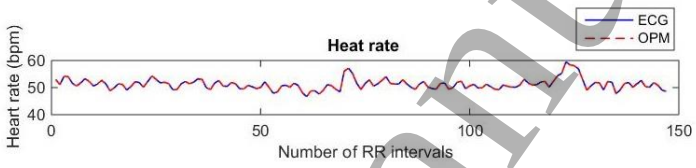

Figure 8: Heart rate determined from simultaneously ECG and OPM recordings.

One heart beat cycle of the real-time pre-filtered ECG/MCG signals and signal-averaged MCG are shown in Figure 9. For the OPM-based data, averaging the cardiac waveform over 15-20 heart beats clearly enhance the signal to noise ratio.

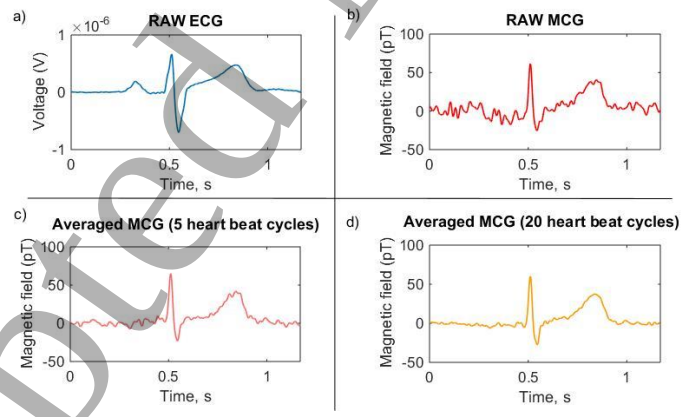

Figure 9: ECG and MCG signals of the healthy 37 years old volunteer. a) Real-time filtered un-averaged ECG signal (one heart beat cycle), b) Real-time filtered un-averaged MCG signal (one heart beat cycle), c) 5 beats averaged MCG signal, d) 20 beats averaged MCG signal.

Quantitative cardiac parameters (heart rate, QRS duration, QT intervals and corrected QT intervals) determined for both healthy volunteers are summarized in Table 2. As previously, detection of QRS duration is based on Pan and Tompkins algorithm (the width of the integrator window is set to 130 ms). QT interval is determined manually using the maximum slope intercept method to define the end of the T wave (Malik and Batchvarov, 2000). QT interval which represents the electrical depolarization and repolarization of the ventricles is dependent on the heart rate (QT lengthens at

slower heart rates) thus a heart-rate corrected QT interval (noted QT_c) is commonly defined. Here, the corrected QT interval is determined using the Bazett's formula: $QT_c = QT/\sqrt{RR}$ with RR the interval from the onset of one QRS complex to the onset of the next one, measured in seconds.

Table 2: Quantitative cardiac parameters for both healthy volunteers determined with ECG and OPMs.

	Subject 1 (male, 47)		Subject 2 (male, 37)	
	ECG	MCG (OPM)	ECG	MCG (OPM)
Heart rate	67beats/min (± 3.8 beats/min)	67 beats/min (± 3.3 beats/min)	51.2 beats/min (±2 beats/min)	
QRS duration	101 ms (±0.2 ms)	105 ms (±3.8 ms)	122 ms (±0.2 ms)	122 ms (±3 ms)
QT interval	370 ms	371 ms	452 ms	453 ms
QT_c	391 ms	392 ms	417 ms	419 ms

Normal QT_c varies between 350 ms and 400 ms, and a long QT syndrome in males is defined for a QT_c above 450 ms. For the 37 years old, the borderline QT_c ($400\ ms < QT_c = 419\ ms < 450\ ms$) is representative of a nonspecific intraventricular conduction delay, which was confirmed by the clinical examination of the patient carried out before the beginning of the clinical trial.

Statistical analysis of the QRS duration is performed with a Student t-test (α=0.05) on ECG and OPM-based MCG data for the 37-years old volunteers. A p-value of 78% is obtained which shows that there is no statistical difference on QRS duration between the ECG and the MCG signal measured with ^{4}He magnetometers.

All these data confirm that the room-temperature vector ^{4}He OPM can record MCG signals and provide reliable information about cardiac activity.

4. Conclusion

MCG measurements performed in a clinical environment on two healthy volunteers confirm that a ^{4}He vector magnetometer operated in a gradiometer mode is a promising sensor to record real-time human MCG signals. An important advantage of ^{4}He OPMs is the possibility of operating the sensor at room temperature without thermal insulation, with a reduced "sensor-subject" distance and a better signal strength. Another key characteristic of the developed ^{4}He OPM is the possibility to record with the same sensor the three components of the MCG signal.

Sensitivity of the ^{4}He OPM is currently limited by the excess noise of our fiber laser at 1083 nm (depending on the frequency and optical power, the RIN is 10-20dB above the RIN shot noise). We expect that sensitivity of our gradiometer will be significantly improved by the ultra-low noise 1083 nm laser diode currently developed. In parallel, future work will concentrate on designing an OPM array dedicated to multichannel MCG/MEG recordings enabling mapping approaches.

This work was supported by the French National Research Agency (ANR) through Carnot funding. The authors thank A. Palacios-Laloy for fruitful discussions on the manuscript.

References:

Alem, O., Sander, T.H., Mhaskar, R., LeBlanc, J., Eswaran, H., Steinhoff, U., Okada, Y., Kitching, J., Trahms, L., Knappe, S., 2015. Fetal magnetocardiography measurements with an array of

microfabricated optically pumped magnetometers. Phys. Med. Biol. 60, 4797–4811. doi:10.1088/0031-9155/60/12/4797

Antzelevitch, C., Shimizu, W., Yan, G.X., Sicouri, S., 1998. Cellular basis for QT dispersion. J. Electrocardiol. 30 Suppl, 168–175.

Bison, G., 2004. Development of an optical cardio-magnetometer (Dissertation). UniversitÄatsdruckerei Freiburg.

Bison, G., Castagna, N., Hofer, A., Knowles, P., Schenker, J.-L., Kasprzak, M., Saudan, H., Weis, A., 2009. A room temperature 19-channel magnetic field mapping device for cardiac signals. Appl. Phys. Lett. 95, 173701. doi:10.1063/1.3255041

Bison, G., Stumpf, M., Lembke, G., 2010. Design of a 57 Channel Optical Biomagnetometersystem. Biomed. Tech. 55, 72–4. doi:10.1515/BMT.2010.293

Cohen-Tannoudji, C., Dupont-Roc, J., Haroche, S., Laloë, F., 1970a. Diverses résonances de croisement de niveaux sur des atomes pompés optiquement en champ nul II. Applications à la mesure de champs faibles. Rev. Phys. Appl. 5, 102–108. doi:10.1051/rphysap:0197000501010200

Cohen-Tannoudji, C., Dupont-Roc, J., Haroche, S., Lalöe, F., 1970b. Diverses résonances de croisement de niveaux sur des atomes pompés optiquement en champ nul I. Théorie. Rev Phys Appl 5, 95–101.

Cuneo, B.F., Strasburger, J.F., Yu, S., Horigome, H., Hosono, T., Kandori, A., Wakai, R.T., 2013. In utero diagnosis of long QT syndrome by magnetocardiography. Circulation 128, 2183–2191. doi:10.1161/CIRCULATIONAHA.113.004840

Dupont-Roc, J., 1971. Étude théorique de diverses résonances observables en champ nul sur des atomes “ habillés ” par des photons de radiofréquence. J. Phys. 32, 135–144. doi:10.1051/jphys:01971003202-3013500

Dupont-Roc, J., 1970. Détermination par des méthodes optiques des trois composantes d’un champ magnétique très faible. Rev. Phys. Appliquée 5, 853–864. doi:10.1051/rphysap:0197000506085300

Dupont-Roc, J., Haroche, S., Cohentan.c, 1969. Detection of Very Weak Magnetic Fields (10-9gauss) by 87rb-Zero-Field Level Crossing Resonances. Phys. Lett. A A 28, 638–&. doi:10.1016/0375-9601(69)90480-0

Durrer, D., van Dam, R.T., Freud, G.E., Janse, M.J., Meijler, F.L., Arzbaecher, R.C., 1970. Total excitation of the isolated human heart. Circulation 41, 899–912.

Elgendi, M., 2013. Fast QRS Detection with an Optimized Knowledge-Based Method: Evaluation on 11 Standard ECG Databases. PLOS ONE 8, e73557. doi:10.1371/journal.pone.0073557

Fenici, R., Brisinda, D., Venuti, A., Sorbo, A.R., 2013. Thirty years of clinical magnetocardiography at the Catholic University of Rome: diagnostic value and new perspectives for the treatment of cardiac arrhythmias. Int. J. Cardiol. 168, 5113–5115. doi:10.1016/j.ijcard.2013.07.238

Fourcault, W., Leger, J.M., Costes, V., Fratter, I., Mondin, L., 2010. ATHERMAL FIBER LASER FOR THE SWARM ABSOLUTE SCALAR MAGNETOMETER. Presented at the ICSO 2010, International Conference on Space Optics, Rhodes, Greece.

Fujino, K., Sumi, M., Saito, K., Murakami, M., Higuchi, T., Nakaya, Y., Mori, H., 1984. Magnetocardiograms of patients with left ventricular overloading recorded with a second-derivative SQUID gradiometer. J. Electrocardiol. 17, 219–228.

Ikefuji, H., Nomura, M., Nakaya, Y., Mori, T., Kondo, N., Ieishi, K., Fujimoto, S., Ito, S., 2007. Visualization of cardiac dipole using a current density map: detection of cardiac current undetectable by electrocardiography using magnetocardiography. J. Med. Investig. JMI 54, 116–123.

Kandori, A., Shimizu, W., Yokokawa, M., Noda, T., Kamakura, S., Miyatake, K., Murakami, M., Miyashita, T., Ogata, K., Tsukada, K., 2004. Identifying patterns of spatial current dispersion that characterise and separate the Brugada syndrome and complete right-bundle branch block. Med. Biol. Eng. Comput. 42, 236–244.

Knappe, S., Sander, T.H., Kosch, O., Wiekhorst, F., Kitching, J., Trahms, L., 2010. Cross-validation of microfabricated atomic magnetometers with superconducting quantum interference devices for biomagnetic applications. Appl. Phys. Lett. 97, 133703. doi:10.1063/1.3491548

Koch, H., Haberkorn, W., 2001. Magnetic field mapping of cardiac electrophysiological function. Philos. Trans. R. Soc. Lond. Math. Phys. Eng. Sci. 359, 1287–1298. doi:10.1098/rsta.2001.0831

Kwong, J.S.W., Leithäuser, B., Park, J.-W., Yu, C.-M., 2013. Diagnostic value of magnetocardiography in coronary artery disease and cardiac arrhythmias: a review of clinical data. Int. J. Cardiol. 167, 1835–1842. doi:10.1016/j.ijcard.2012.12.056

Le Prado, M., 2014. Conception, réalisation et application d'un magnétomètre atomique vectoriel (Dissertation). Université de Franche-Comté UFC.

Lembke, G., Erné, S.N., Nowak, H., Menhorn, B., Pasquarelli, A., 2014. Optical multichannel room temperature magnetic field imaging system for clinical application. Biomed. Opt. Express 5, 876–881. doi:10.1364/BOE.5.000876

Livanov, M.N., Koslov, A.N., Sinelnikova, S.E., Kholodov, J.A., Markin, V.P., Gorbach, A.M., Korinewsky, A.V., 1981. Record of the human magnetocardiogram by the quantum gradiometer with optical pumping. Adv. Cardiol. 28, 78–80.

Malik, M., Batchvarov, V.N., 2000. Measurement, interpretation and clinical potential of QT dispersion. J. Am. Coll. Cardiol. 36, 1749–1766. doi:10.1016/S0735-1097(00)00962-1

Mäntynen, V., Konttila, T., Stenroos, M., 2014. Investigations of sensitivity and resolution of ECG and MCG in a realistically shaped thorax model. Phys. Med. Biol. 59, 7141–7158. doi:10.1088/0031-9155/59/23/7141

McSharry, P.E., Clifford, G.D., Tarassenko, L., Smith, L.A., 2003. A dynamical model for generating synthetic electrocardiogram signals. IEEE Trans. Biomed. Eng. 50, 289–294. doi:10.1109/TBME.2003.808805

OROS, 2009. NVGate®, Sofware Platform for OROS 3-Series, Technical specifications, www.oros.com.

Pan, J., Tompkins, W.J., 1985. A Real-Time QRS Detection Algorithm. IEEE Trans. Biomed. Eng. BME-32, 230–236. doi:10.1109/TBME.1985.325532

Pannetier-Lecoeur, M., Parkkonen, L., Sergeeva-Chollet, N., Polovy, H., Fermon, C., Fowley, C., 2011. Magnetocardiography with sensors based on giant magnetoresistance. Appl. Phys. Lett. 98, 153705. doi:10.1063/1.3575591

Park, J.-W., Hill, P.M., Chung, N., Hugenholtz, P.G., Jung, F., 2005. Magnetocardiography predicts coronary artery disease in patients with acute chest pain. Ann. Noninvasive Electrocardiol. 10, 312–323. doi:10.1111/j.1542-474X.2005.00634.x

PhysioNet, 2015. ECGSYN: A realistic ECG waveform generator (https://www.physionet.org/physiotools/ecgsyn/).

Rutkowski, J., Fourcault, W., Bertrand, F., Rossini, U., Getin, S., Le Calvez, S., Jager, T., Herth, E., Gorecki, C., Le Prado, M., Leger, J.M., Morales, S., 2014. Towards a miniature atomic scalar magnetometer using a liquid crystal polarization rotator. Sens. Actuators -Phys. 216, 386–393. doi:10.1016/j.sna.2014.05.003

Shah, V.K., Wakai, R.T., 2013. A compact, high performance atomic magnetometer for biomedical applications. Phys. Med. Biol. 58, 8153–8161. doi:10.1088/0031-9155/58/22/8153

Sternickel, K., Braginski, A.I., 2006. Biomagnetism using SQUIDs: status and perspectives. Supercond. Sci. Technol. 19, S160–S171. doi:10.1088/0953-2048/19/3/024

Takeuchi, A., Watanabe, K., Nomura, M., Ishihara, S., Sumi, M., Murakami, M., Saito, K., Nakaya, Y., Mori, H., 1988. The P wave in the magnetocardiogram. J. Electrocardiol. 21, 161–167.

Wikswo, J.P., Barach, J.P., 1982. Possible sources of new information in the magnetocardiogram. J. Theor. Biol. 95, 721–729.

Wyllie, R., IV, 2012. The development of a multichannel atomic magnetometer array for fetal magnetocardiography (Dissertation). University of Wisconsin-Madison.

Wyllie, R., Kauer, M., Smetana, G.S., Wakai, R.T., Walker, T.G., 2012. Magnetocardiography with a modular spin-exchange relaxation-free atomic magnetometer array. Phys. Med. Biol. 57. doi:10.1088/0031-9155/57/9/2619

Xia, H., Baranga, A.B.-A., Hoffman, D., Romalis, M.V., 2006. Magnetoencephalography with an atomic magnetometer. Appl. Phys. Lett. 89, 211104. doi:10.1063/1.2392722